


Article

Boosting Lithium Storage of a Metal-Organic Framework via Zinc Doping

Wenshan Gou¹, Zhao Xu¹, Xueyu Lin^{2,*}, Yifei Sun¹, Xuguang Han¹, Mengmeng Liu¹ and Yan Zhang^{1,*} 

¹ Institute of Advanced Cross-Field Science, College of Life Sciences, Qingdao University, Qingdao 200671, China; 2019025181@qdu.edu.cn (W.G.); 2019025203@qdu.edu.cn (Z.X.); 2020025520@qdu.edu.cn (Y.S.); 2020025501@qdu.edu.cn (X.H.); 2020025500@qdu.edu.cn (M.L.)

² Beijing National Laboratory for Molecular Sciences and State Key Laboratory of Rare Earth Materials Chemistry and Applications, College of Chemistry and Molecular Engineering, Peking University, Beijing 100871, China

* Correspondence: 1801110301@pku.edu.cn (X.L.); yzhang_iacs@qdu.edu.cn (Y.Z.)

Abstract: Lithium-ion batteries (LIBs) as a predominant power source are widely used in large-scale energy storage fields. For the next-generation energy storage LIBs, it is primary to seek the high capacity and long lifespan electrode materials. Nickel and purified terephthalic acid-based MOF (Ni-PTA) with a series amounts of zinc dopant (0, 20, 50%) are successfully synthesized in this work and evaluated as anode materials for lithium-ion batteries. Among them, the 20% atom fraction Zn-doped Ni-PTA (Zn_{0.2}-Ni-PTA) exhibits a high specific capacity of 921.4 mA h g⁻¹ and 739.6 mA h g⁻¹ at different current densities of 100 and 500 mA g⁻¹ after 100 cycles. The optimized electrochemical performance of Zn_{0.2}-Ni-PTA can be attributed to its low charge transfer resistance and high lithium-ion diffusion rate resulting from expanded interplanar spacing after moderate Zn doping. Moreover, a full cell is fabricated based on the LiFePO₄ cathode and as-prepared MOF. The Zn_{0.2}-Ni-PTA shows a reversible specific capacity of 97.9 mA h g⁻¹ with 86.1% capacity retention (0.5 C) after 100 cycles, demonstrating the superior electrochemical performance of Zn_{0.2}-Ni-PTA anode as a promising candidate for practical lithium-ion batteries.

Keywords: metal-organic frameworks; zinc-ions doped; energy storage and conversion; lithium-ion batteries



Citation: Gou, W.; Xu, Z.; Lin, X.; Sun, Y.; Han, X.; Liu, M.; Zhang, Y. Boosting Lithium Storage of a Metal-Organic Framework via Zinc Doping. *Materials* **2022**, *15*, 4186. <https://doi.org/10.3390/ma15124186>

Academic Editor: Alessandro Dell'Era

Received: 2 May 2022

Accepted: 9 June 2022

Published: 13 June 2022

Publisher's Note: MDPI stays neutral with regard to jurisdictional claims in published maps and institutional affiliations.



Copyright: © 2022 by the authors. Licensee MDPI, Basel, Switzerland. This article is an open access article distributed under the terms and conditions of the Creative Commons Attribution (CC BY) license (<https://creativecommons.org/licenses/by/4.0/>).

1. Introduction

Lithium-ion batteries (LIBs), due to their high energy density, low cost and long lifespan, have been regarded as critical energy storage devices for electric vehicles, large-scale electricity storage, etc. [1]. The scientific concern with lithium-ion batteries is developing cathodes, anodes, and electrolytes [2,3]. The performance of anode material has become a restriction for high-energy LIBs. As we know, an ideal electrode material should possess both high lithium-ions storage capacity and stable electrochemical performance. The commercial anode material graphite, which can be easily produced, is limited by an insufficient capacity of 372 mA h g⁻¹ [4]. Other types of anode materials such as alloy [5,6] and conversion reaction-based transition metal oxides [7,8] possess ultrahigh specific capacity. Nevertheless, the dramatic volume expansion during the charge/discharge process and poor cycle performance restrict the broad use of those materials. Therefore, it is significant to explore novel anode materials with excellent performances for the further development of LIBs.

Metal-organic frameworks (MOFs), as a class of porous materials combining metal ions or clusters with organic linkers through coordination bonds, with a huge variety of structures, large surface areas and adjustable porosity, are widely used in many fields such as gas storage [9], chemical sensors [10], catalysis [11], and drug delivery [12]. Over the past several years, different MOFs have been applied in the secondary battery field, especially

in LIBs [13,14]. Generally, the use of MOFs material in the LIBs field can be classified into two aspects, using MOFs as templates to produce homogeneous metal oxide materials and carbon materials for LIBs [14–16], and using MOFs as electrode materials directly [17–19]. Chen's group first explored MOF-177 with different morphologies as an anode material for LIBs even though the electrochemical performance of MOF-177 was not promising [18]. After that, more and more MOFs have been investigated as electrode materials for LIBs. For instance, Wang et al. synthesized a Co-based coordination polymer nanowire with a specific capacity of 1132 mA h g⁻¹ at a current density of 100 mA g⁻¹ [19]. However, most of the works mentioned above focus on introducing novel MOF electrodes for LIBs. Research about the modification of MOFs to improve their inherent property (such as poor electronic conductivity) and electrochemical performances are still scarce [20]. As we all know, element doping is a regular modification to enhance the electronic conductivity and improve the electrochemical performances of electrode materials. Previous similar works could be found in LiFePO₄ [21,22] and several metal–oxides systems [23]. In this respect, the modification of MOFs by doping should be an effective and practical way to enhance their electrochemical performance. Purified terephthalic acid (PTA) is an optimized ligand used in the synthesis of MOFs due to its easy availability from cheap poly-ethylene terephthalate (PET) plastic products. The purified terephthalic acid-based MOF (Ni-PTA) is a prospective anode material for LIBs due to its unique layered structure. However, the performances of Ni-PTA need to be further elevated by optimizing its fine structure (such as interlayer spacing) to realize the high diffusion of Li⁺ [16].

Compared to Ni²⁺ (0.065 nm), Zn²⁺ owns a larger radius (0.074 nm), and the doping of Zn²⁺ can expand the interplanar distances of Ni-PTA, which facilitates the diffusion of Li⁺. Herein, we successfully synthesized a series of nickel and purified terephthalic acid-based MOF (Ni-PTA) with different amounts of zinc doping (the x% atom fraction Zn-doped Ni-PTA was denoted as Zn_x-Ni-PTA) through a simple solvothermal method and explored them as anode materials for LIBs. The result shows that Zn_{0.2}-Ni-PTA achieves more excellent cycle stability and higher specific capacity than the Ni-PTA without Zn-doped and the 50% atom fraction Zn-doped (Zn_{0.5}-Ni-PTA) one. The further kinetics information reveals that the Zn_{0.2}-Ni-PTA demonstrates a faster Li⁺ diffusion rate and lower charge transfer resistance, which also explains the brilliant electrochemical performance of Zn_{0.2}-Ni-PTA. In addition, we fabricated a full cell based on a LiFePO₄ cathode to test the electrochemical performance of Zn_{0.2}-Ni-PTA as anode.

2. Materials and Methods

2.1. Synthesis of Zn_x-Ni-PTA

The Zn_x-Ni-PTA was prepared by a simple one-pot solvothermal route. Briefly, 0.166 g of purified terephthalic acid (PTA, Aladdin, 99%), 1.5/1.2/0.75 mmol of Ni(NO₃)₂·6H₂O (Aladdin, analytically pure) and different amounts of Zn(NO₃)₂·6H₂O (Aladdin, analytically pure) (0, 0.3, 0.75 mmol) were, respectively, dissolved in a mixed solvent consisting of 15 mL absolute ethanol (Macklin, analytically pure) and 15 mL deionized H₂O, which was then stirred for 30 min. Then, the mixture was transformed into a 40 mL Teflon-lined stainless steel autoclave and reacted at 180 °C for 24 h. After the autoclave cooled down to room temperature, the green precipitates were washed by N,N-dimethylformamide (DMF, Aladdin, analytically pure) and absolute ethanol several times. Ultimately, this product was dried at 60 °C in air for 24 h. The 0%, 20% and 50% atom fraction Zn-doped Ni-PTA denoted Zn₀-Ni-PTA, Zn_{0.2}-Ni-PTA, and Zn_{0.5}-Ni-PTA, respectively.

2.2. Materials Characterization

The powder X-ray diffraction (XRD) patterns were recorded by a Rigaku II X-ray diffraction spectrometer (Japan Science Co., Tokyo, Japan) using Cu-K α radiation. Fourier-transform infrared (FTIR) transmission spectra were performed by FTIR-65 IR spectrophotometer (Tianjin Port East Technology Co., Tianjin, China). Thermogravimetric–Differential Thermal Analysis (TG-DTA) was performed by a Labsys Evo thermogravimetric differential

thermal analyzer from the Setaram Instrumentation (France) with a rate of 10 K min^{-1} under ambient condition. The JSM-JSM7500 instrument (Japan Electronics Co., Tokyo, Japan) obtained scanning electron microscopy (SEM) images. X-ray photoelectron spectroscopy (XPS) was taken on the PHI5000VersaProbe instrument (Shanghai Yuzhong Industrial Co., Shanghai, China). Inductively Coupled Plasma–Atomic Emission Spectrometry (ICP-AES) record was obtained by ICP-9000(N+M) atomic emission spectroscopy (Thermo Jarrel-Ash Co., Boston, MA, USA).

2.3. Electrochemical Measurements

To carry out the electrochemical measurements, the active material, Super-P carbon black and polyvinyl difluoride (PVDF, Macklin, $M_w = 1,000,000$) were blended in a weight ratio of 6:3:1 with several drops of N-methyl pyrrolidone (NMP) added and stirred until the mixture became homogeneous. Afterward, the mixed slurry was pasted onto a copper foil current collector with a diameter of 10 mm and dried in vacuum at $80\text{ }^\circ\text{C}$ for 12 h. The average loading of active materials was about 1.2 mg cm^{-1} . The CR 2016-type cells were assembled in an Ar-filled glove box (water and oxygen concentration less than 0.1 ppm), using lithium foil as the counter electrode and Celgard 2300 polypropylene as separators (diameter—16 mm). The electrolyte was 1 M LiPF_6 dissolved in a solvent mixed with EC-DMC-EMC (1:1:1 vol %). The galvanostatic charge–discharge (GCD) tests were performed by a LAND CT2001 battery test system (Wuhan Kingnuo Electronic Co., Wuhan, China) at room temperature ($25\text{ }^\circ\text{C}$). Cycle voltammetry (CV) and electrochemical impedance spectroscopy (EIS) were taken on a CHI-660B electrochemical station (Shanghai Chenhua Instrument Co., Shanghai, China) at a full charge state of batteries after the 20th cycle. The current density of test is 0.1 A g^{-1} . The CV tests were carried out with a scan rate of 0.1 mV s^{-1} , while the EIS data were recorded in the frequency range of 0.01–100 kHz. The full cell was similarly assembled as above-mentioned: 20 at % Zn-doped Ni-PTA as anode, and the cathode was obtained by homogeneously mixing the LiFePO_4 (Canrd, D-1, 80 wt %), PVDF (10 wt %) and NMP (10 wt %). The loading density was about 0.4 mg cm^{-2} , and Al foil was used as the current collector. The specific capacity was calculated based on the cathode material.

3. Results and Discussion

3.1. Characterization of $\text{Zn}_x\text{-Ni-PTA}$

To investigate the crystalline phase of as-prepared products, XRD measurement was performed. Figure 1a shows the XRD patterns of $\text{Zn}_x\text{-Ni-PTA}$ with different amounts of zinc doping and the standard card of $\text{Ni}_3(\text{OH})_2(\text{C}_8\text{H}_4\text{O}_4)_2 \cdot (\text{H}_2\text{O})_4 \cdot 2\text{H}_2\text{O}$ (CCDC 638866) belonging to the space group of P-1(2)-triclinic. Although all the XRD patterns of synthesized MOFs shared similarities, with the increasing Zn^{2+} amount, the peaks of (010) and (020) tend to become invisible. This phenomenon illustrates that the crystal structure order along the *b*-axis decreased. In addition to the absence of some reflections, with the amount of zinc dopant increasing, the peaks of (100) and (200) shifted to a lower angle, which can be attributed to the partial replacement of doped larger Zn^{2+} (0.074 nm) to Ni^{2+} (0.065 nm) in MOFs, expanding the interplanar distances along the *a*-axis [24,25]. The SEM images of $\text{Zn}_x\text{-Ni-PTA}$ are presented in Figure S1. The $\text{Zn}_0\text{-Ni-PTA}$ showed layered micro-sheet like morphology features, and the flower-like layered structure was observed after Zn^{2+} doping. TGA curves (Figure S2) indicates that the initial weight loss is due to the loss of solvated water molecules and the weight loss in the range of $350\text{--}420\text{ }^\circ\text{C}$ is attributed to the thermal decomposition of the $\text{Zn}_x\text{-Ni-PTA}$.

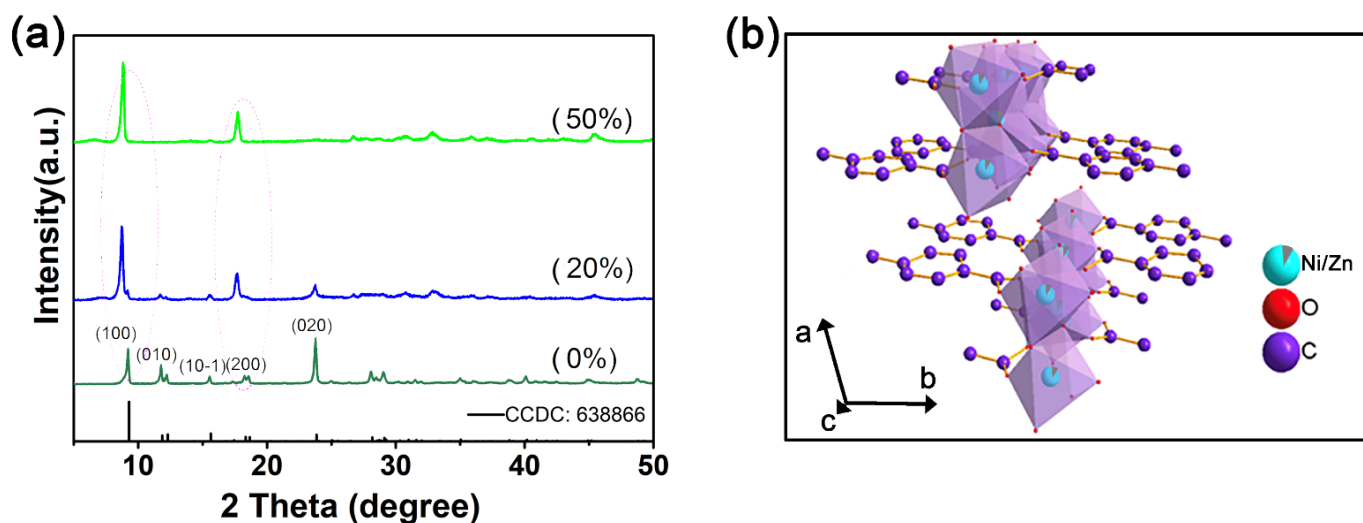


Figure 1. (a) Powder XRD pattern of the different atom fraction Zn_x -Ni-PTA samples. (b) The structure mode of Zn_x -Ni-PTA.

In addition, the similar FTIR peaks also proved that these synthesized MOFs have similar layered topology crystal structures, as shown in Figure 2a. According to the patterns, bands at 1501 cm^{-1} reveal the para-aromatic C-H stretching mode. The bending stretching vibration of -OH is observed at 3613 cm^{-1} . The bands at 3070 cm^{-1} , 3344 cm^{-1} and 3431 cm^{-1} are assigned to stretching vibrations of H_2O in MOFs. In addition, the asymmetric and symmetric vibration of COO^- are located at 1581 cm^{-1} and 1400 cm^{-1} , respectively. The more Zn content, the larger of COO^- groups separation that demonstrated the impact of doped zinc ions on the structure of MOF. The absorption peaks at 522 cm^{-1} in $Zn_{0.2,0.5}$ -Ni-PTA are associated to Ni-O, and peaks at 437 cm^{-1} in $Zn_{0.2,0.5}$ -Ni-PTA are associated to Zn-O vibration bonds, respectively [26,27]. This also confirms the successful doping of Zn^{2+} to the Ni-PTA. The content of dopant Zn^{2+} in Zn_x -Ni-PTA samples (0%, 22.06% and 50.83%) was detected by induced coupled plasma atomic emission spectroscopy (ICP-AES), respectively (Table S1) and matched well with the theoretical value. The above results indicated that different amounts of Zn^{2+} successfully replaced the Ni^{2+} in Ni-MOFs.

For further information about elemental composition and valance state, an XPS test was performed. As observed from the XPS spectra of Zn 2p (Figure 2b), no characteristic peaks were detected in the Zn_0 -Ni-PTA sample, and two prominent doublet peaks corresponding to Zn $2p_{1/2}$ and Zn $2p_{3/2}$ can be observed in $Zn_{0.2}$ -Ni-PTA and $Zn_{0.5}$ -Ni-PTA, indicating the successful doping of Zn in these two samples [28]. In the Ni 2p spectra (Figure 2c) of Zn_x -Ni-PTA, all samples share similar peak types attributed to Ni^{2+} , but the binding energy shows the obvious difference before and after doping. The binding energy of Ni $2p_{3/2}$ in pristine Ni-PTA (Zn_0 -Ni-PTA) is 855.8 eV; by contrast, the value shifts to 858.2 and 857.9 eV in $Zn_{0.2}$ -Ni-PTA and $Zn_{0.5}$ -Ni-PTA. Such difference perhaps originates from that the doped Zn^{2+} with different electronegativity influences the electronic interactions of Ni^{2+} [29,30]. Based on the discussion above, it can be inferred that Zn^{2+} has strong bands with organic ligands in MOFs. All of the evidence discussed above proved the successful doping of zinc. The surface area (BET) data of different Zn_x -Ni-MOF are display in Table S2.

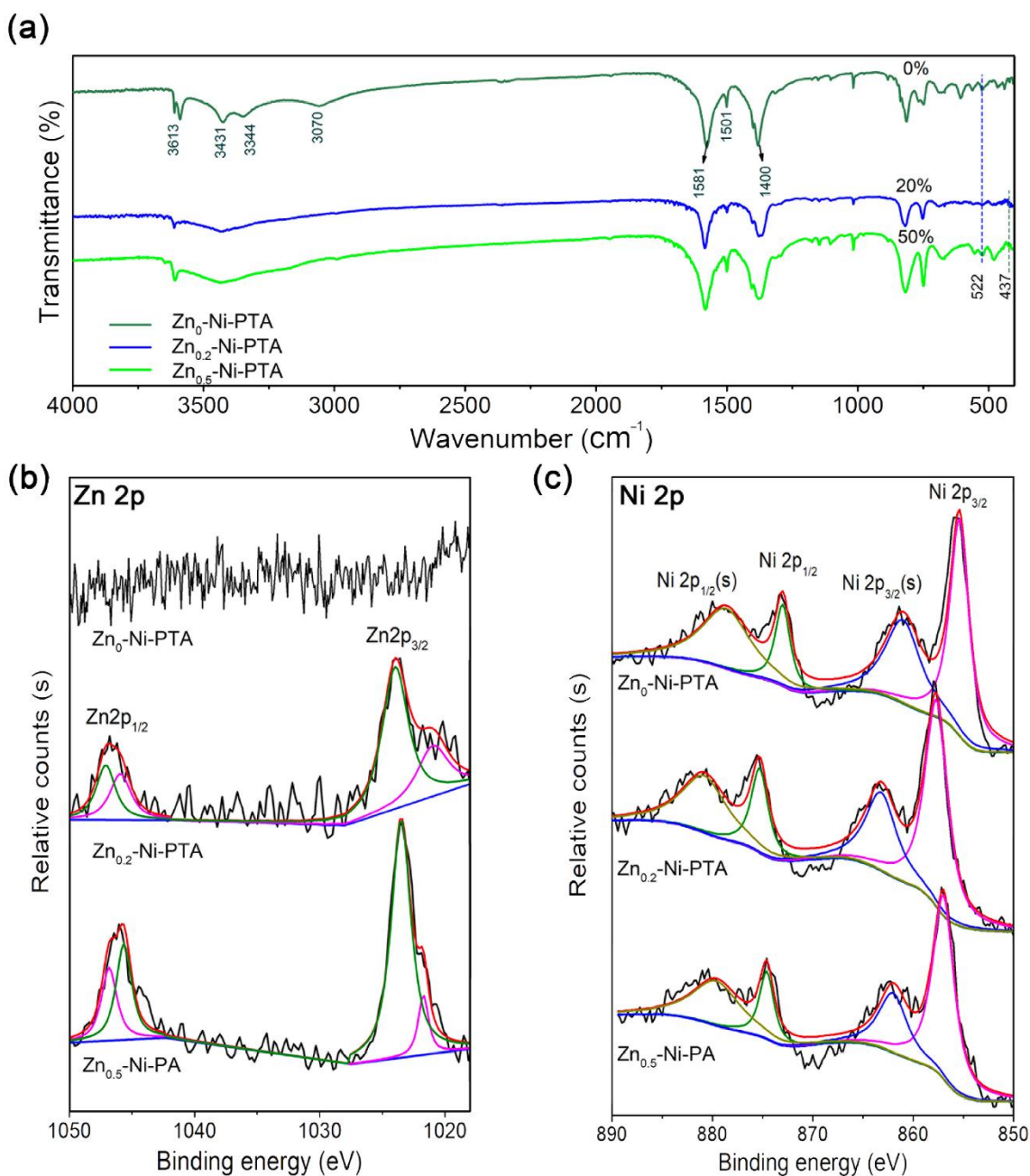


Figure 2. (a) FTIR pattern of the different atom fraction Zn_x-Ni-PTA samples. (b) Zn 2p and (c) Ni 2p spectra of Zn_x-Ni-PTA.

3.2. Half-Cell Test

To investigate the Li-ion storage capacity of Zn_{0.2}-Ni-PTA, electrochemical tests were performed and are shown in Figure 3. The CV curves, as shown in Figure 3a, exhibit a weak reduction peak at about 1.30 V and a sharp reduction peak at 0.75 V followed by a broad oxidation peak around 1.25 V during the initial anodic scan, which can be ascribed to the lithiation/de-lithiation of carboxylate groups and aromatic rings and the formation of a solid-electrolyte interphase (SEI) layer [31,32]. Compared with the first cycle, the intensity of the redox peaks in the second and third cycles are growing weaker, which is related to structural or morphological evolution [33]. The sharp redox peaks shift toward higher/lower potential (≈0.75/1.40 V), which corresponds to the Li-ions insertion/extraction into/from the carboxylate groups and the benzene rings of Zn_x-Ni-PTA [34]. Notably, Zn₀-Ni-PTA, Zn_{0.2}-Ni-PTA, and Zn_{0.5}-Ni-PTA showed similar CV curves

(Figure S3 left). This phenomenon implies that zinc dopant did not change the topology of pristine MOF; instead, it only just boosted lithium storage performance. The charge–discharge curves of the $\text{Zn}_{0.2}\text{-Ni-PTA}$ are shown in Figure 3b. Two discharge voltage plateaus at about 1.30 V and 0.75 V could be observed in the first discharge curve. Then, following the charging process, two charge ranges are demonstrated, which agree well with the CV curves. Combining with the subsequent cycles, we can assume that the reversible discharge plateau of $\text{Zn}_{0.2}\text{-Ni-PTA}$ at 1.0–0.5 V contributes the most capacity.

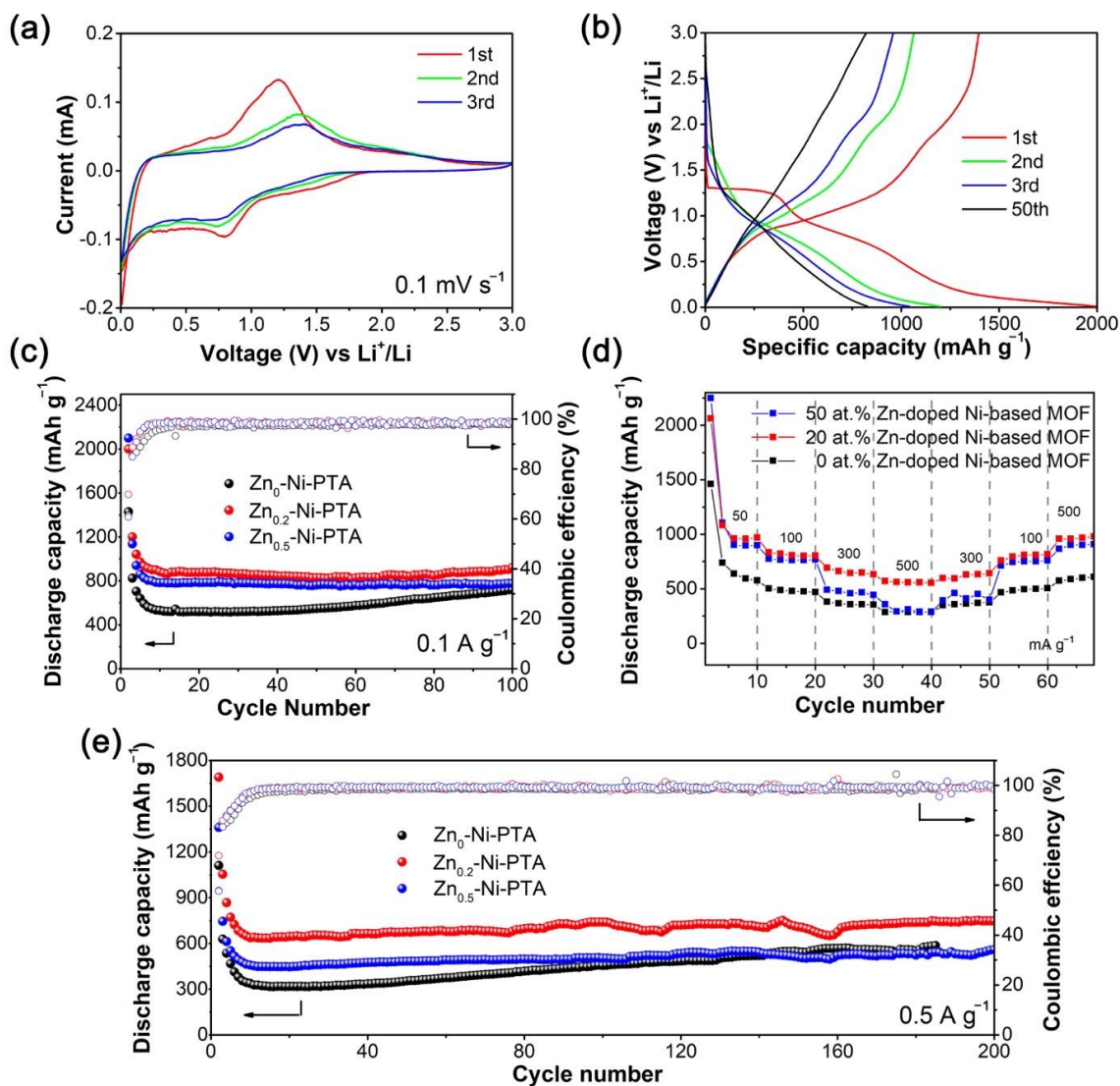


Figure 3. Electrochemical performance of $\text{Zn}_x\text{-Ni-PTA}$ material: (a) CV curves and (b) voltage profiles of 20% atom fraction Zn-doped Ni-PTA. (c,e) Cycle and (d) rate performance of different MOFs.

The cycle performance of different amounts of Zn-doped Ni-PTA at the current density 0.1 A g^{-1} and 0.5 A g^{-1} is displayed in Figure 3c,e. The 20% atom fraction Zn-doped Ni-PTA delivers the initial discharge capacity of 2000 mA h g^{-1} at 0.1 A g^{-1} and 1690 mA h g^{-1} at 0.5 A g^{-1} . After 100/200 cycles, the discharge capacity retains up to 921 and 747 mA h g^{-1} at $0.1 \text{ A g}^{-1}/0.5 \text{ A g}^{-1}$, respectively, with a Coulombic efficiency of nearly 100%. We are noticing that the capacity of three samples mildly increases after about the 10th cycle, which might be due to the electrochemical activation process related to the repeated insertion/extraction of Li-ions in MOFs. In simple terms, during charging and discharging, the inserted Li^+ expanded the interlayer spacing of samples and exposed a larger number of active sites, which could be beneficial for gradually increasing capacity. In addition, it

is clear that the cycle performance of Zn_{0.2}-Ni-PTA is superior to the other two MOFs. In addition, the better rate performance of Zn_{0.2}-Ni-PTA is exhibited in Figure 3d. In summary, the reversible capacity at current density values of 50, 100, 300, and 500 mA g⁻¹ is 958, 806, 646, and 556 mA h g⁻¹, respectively. Moreover, when the current density decreases to 50 mA g⁻¹, the discharge capacity remains stable.

Based on the above electrochemical tests, combined with the cycle performance information of different atom fractions of (0, 10, 20, 30, 40, 50%) Zn-doped Ni-PTA (Figure S5), we can prove that Zn_{0.2}-Ni-PTA displays the best electrochemical performance among different atom fractions of zinc doped Ni-PTA samples. For comparison, their electrochemical performances are presented along with the other MOFs in Table S3. In addition, the XRD patterns and SEM images of Zn_{0.2}-Ni-PTA electrodes before and after the cycle are displayed in Figure S4. The SEM images show that Zn_{0.2}-Ni-PTA maintains its pristine microplate-like characteristics after cycles, indicating its good morphological stability. Interestingly, an amorphization process after cycles is determined by XRD. This phenomenon perhaps originates from the electrochemical powderization effect due to the repeat insertion/extraction of Li⁺ in its crystal [35]. Such an amorphization process was also observed in other lithium storage cases of MOFs materials [33,35]. Moreover, the decrease in redox peaks in the first few cycles observed from CV curves may be also related to this amorphization process.

3.3. Electrochemical Analysis

To better understand why Zn_{0.2}-Ni-PTA possesses brilliant electrochemical performance, the effect of doped Zn²⁺ on the migration of Li⁺ was also investigated. It is well known that the high migration rate of lithium-ions can improve the electrochemical performance of the battery [36–38]. Therefore, electrochemical impedance spectroscopy (EIS) experiments are conducted to explore the kinetics. From the Nyquist diagrams, as shown in Figure 4a, it is shown that Zn_{0.2}-Ni-PTA possesses a lower electrochemical impedance than Zn₀-Ni-PTA. Furthermore, the chemical diffusion coefficient of Li⁺ (D_{Li^+}) was calculated by Equation (1). R , T , A , F , n , and C are the ideal gas constant, the thermal-dynamic temperature, the surface area of electrodes, the Faraday's constant, the number of electrons per molecule during oxidation, and the Li⁺ concentration in the cathode, respectively. The σ_W is the Warburg coefficient, which has a linear relation with Z' (Equation (2)):

$$D_{Li^+} = \left(\frac{2RT}{\sqrt{2}n^2F^2\sigma_W AC} \right)^2 = \frac{2R^2T^2}{n^4F^4\sigma_W^2 A^2 C^2} \quad (1)$$

$$Z' = R_s + R_{ct} + \sigma_W \omega^{-1/2} \quad (2)$$

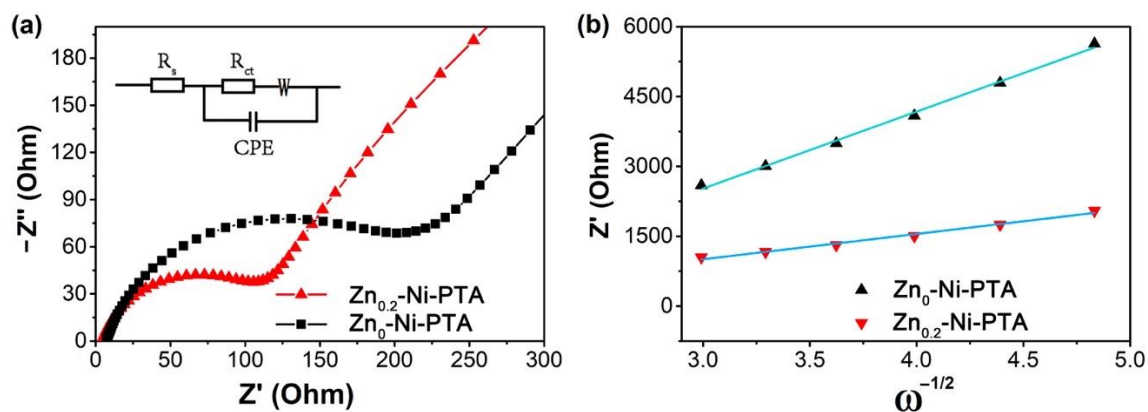


Figure 4. (a) Nyquist plot of Zn_{0.2}-Ni-PTA and Zn₀-Ni-PTA. (b) Z' vs. $\omega^{-1/2}$ plots in low frequency region.

In Equation (2), R_s and R_{ct} represent the resistance of solution and the charge transfer, respectively [25]. Figure 4b illustrates the linear relationship plot of $\omega^{-1/2}$ (reciprocal square root of angular frequency) vs. Z' (actual impedance) in the low frequency of Zn_x -Ni-PTA. The slope of this linear plot is equal to the value of σ_W . As shown clearly in the plot, by contrast with Zn_0 -Ni-PTA, $Zn_{0.2}$ -Ni-PTA possess a smaller slope, which demonstrates a higher Li^+ diffusion coefficient and better electrochemical performance. Compared to Ni^{2+} (0.065 nm), Zn^{2+} has a larger radius (0.074 nm), and the doped Zn^{2+} expands the interplanar distances of $Zn_{0.2}$ -Ni-PTA, which facilitates the diffusion of Li^+ . Thus, $Zn_{0.2}$ -Ni-PTA displays a higher Li^+ diffusion coefficient and improved lithium storage performances [39].

3.4. Full-Cell Test

To further investigate the application prospects of the sample, we constructed the full cell using Zn_x -Ni-PTA as anode coupled with $LiFePO_4$ as cathode. The electrochemical test is performed at a voltage range of 0.5–4.0 V. Figure 5a shows the charge and discharge curves of the $Zn_{0.2}$ -Ni-PTA/ $LiFePO_4$ full cell. It yields a discharge capacity of $113.7 \text{ mA h g}^{-1}$ with an average operation voltage of around 2.6 V at 0.5 C. At 0.1 C, 0.5 C, 1 C, 2 C, and 5 C, the reversible capacity remains 124.5, 105.9, 82.2, 62.4, and 50.3 mA h g^{-1} , respectively (Figure 5b). After 200 cycles, the capacity still retains 94.7 mA h g^{-1} with a high capacity retention of 83.24%, which contrasted sharply with the terrible cycle performance of Ni-PTA without Zn doped (Figure 5c). It should be mentioned that the mass loading of $LiFePO_4$ was relatively lower in this work compared to that in commercial LIBs. For most lab-level research, the mass loading of active materials is also lower [40]. In consideration of practical application, we will try modifying the loading of LFP in our later research to achieve a higher energy density.

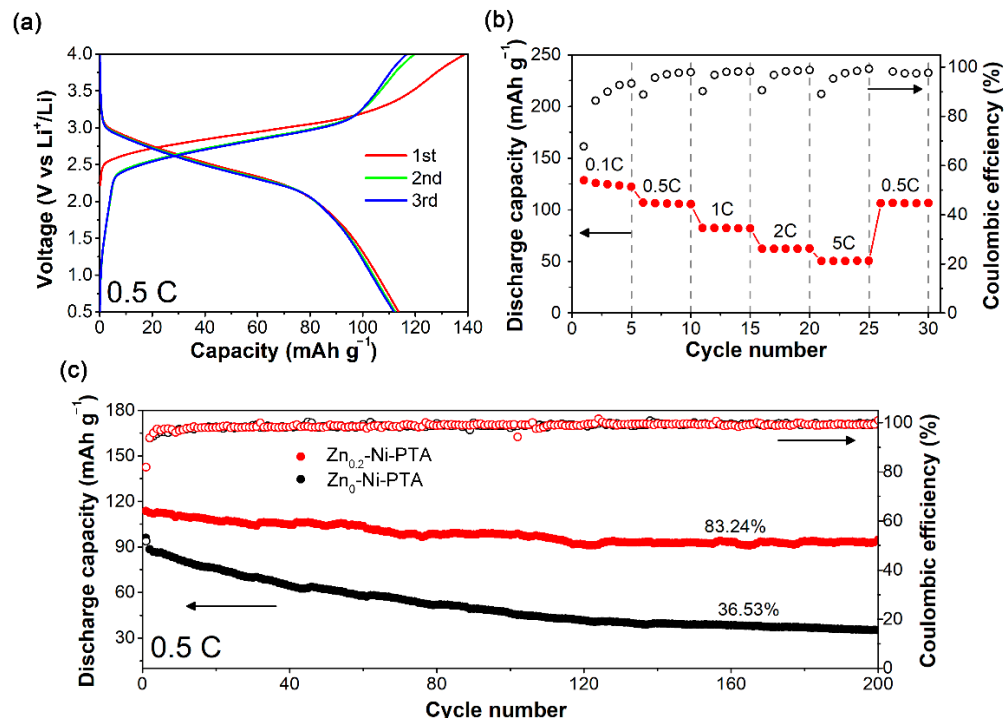


Figure 5. (a) Charge–discharge curves, (b) rate performance and (c) cycle performance of $Zn_{0.2}$ -Ni-PTA/ $LiFePO_4$ full cell.

The above electrochemical result of both half and full cells based on $Zn_{0.2}$ -Ni-PTA with high reversible capacity, safe operation potential, excellent rate and cycle stability is superior to the previous report of synthesized Ni-MOF [16]. This could be attributed to the following aspects: First, the zinc with a large radius can hinder the destruction of the

electrode material and enlarge the interplanar distances [21,24,31,32]. Meanwhile, the EIS results showed that Zn_{0.2}-Ni-PTA delivered less impedance and charge-transfer resistance, bringing a faster Li-ion transmission rate. In summary, Zn_{0.2}-Ni-PTA is a valuable anode material for LIBs.

4. Conclusions

In this work, we successfully synthesized different amounts of Zn doped Ni-PTA and used it as an electrode material for LIBs. In contrast with Ni-PTA, the visible enhancement of lithium storage ability (initial discharge capacity is 2000 mA h g⁻¹ at the current density of 100 mA g⁻¹) and cycle stability (≈85% reversible discharge capacity retained after 100 cycles) are observed in 20% Zn-doped Ni-PTA. The following characterizations indicated that the better performance of samples is because of the higher structural stability and lower impedance and charge-transfer resistance after zinc ions are doped. The work brings new perspectives to the modification of present MOFs electrode materials for LIBs. It may lead us to think about the potential use of Zn_{0.2}-Ni-PTA as anode materials for lithium-ion batteries in the future.

Supplementary Materials: The following supporting information can be downloaded at: <https://www.mdpi.com/article/10.3390/ma15124186/s1>. Figure S1: SEM of the samples, Figure S2: TG-DTA of the (a) 0% Zn-doped Ni-MOF, (b) 20% Zn-doped Ni-MOF, (c) 50% Zn-doped Ni-MOF, Figure S3: CV (left) and charge/discharge curves (right) of the samples, Figure S4: (a,b,c,d) SEM micrograph of electrode, (e) XRD patterns of the electrodes, Figure S5: The cycle performance of different amounts of Zn-doped Ni-PTA, Table S1: Induced coupled plasma atomic emission spectroscopy (ICP-AES) results of the Zn-doped Ni-MOF, Table S2: The surface area (BET) of the Zn_x-Ni-MOF, Table S3: Summary of metal-organic frameworks reported as anode materials in rechargeable lithium-ions batteries. References [41–51] are cited in the supplementary materials.

Author Contributions: Conceptualization, W.G. and Y.Z.; methodology, W.G.; software, W.G. and Z.X.; validation, W.G., Z.X. and Y.S.; formal analysis, W.G. and X.H.; investigation, Z.X. and M.L.; resources, X.L.; data curation, Y.S. and X.H.; writing—original draft preparation, W.G.; writing—review and editing, W.G. and Y.Z.; visualization, X.L. and M.L.; supervision, X.L. and Y.Z.; project administration, Y.Z.; funding acquisition, Y.Z. All authors have read and agreed to the published version of the manuscript.

Funding: This work was supported by Research Start-up Funds of Young Talents from Qingdao University (DC2000003363).

Institutional Review Board Statement: Not applicable.

Informed Consent Statement: Not applicable.

Data Availability Statement: Not applicable.

Conflicts of Interest: The authors declare no conflict of interest.

References

1. Zhu, P.C.; Gastol, D.; Marshall, J.; Sommerville, R.; Goodship, V.; Kendrick, E. A Review of Current Collectors for lithium-ion Batteries. *J. Power Sources* **2021**, *485*, 229321229321. [[CrossRef](#)]
2. Chen, Y.Q.; Kang, Y.Q.; Zhao, Y.; Wang, L.; Liu, J.L.; Li, Y.X.; Liang, Z.; He, X.M.; Li, X.; Tavajohi, N.; et al. A Review of Lithium-ion Battery Safety Concerns: The Issues, Strategies, and Testing Standards. *J. Energy Chem.* **2021**, *59*, 83–99. [[CrossRef](#)]
3. Shen, L.; Wu, H.B.; Liu, F.; Brosmer, J.L.; Shen, G.; Wang, X.; Zink, J.I.; Xiao, Q.; Cai, M.; Wang, G.; et al. Creating Lithium-Ion Electrolytes with Biomimetic Ionic Channels in Metal-Organic Frameworks. *Adv. Mater.* **2018**, *30*, 17074761707476. [[CrossRef](#)] [[PubMed](#)]
4. Chen, J.J.; Mao, Z.Y.; Zhang, L.X.; Tang, Y.H.; Wang, D.J.; Bie, L.J.; Fahlman, B.D. Direct Production of Nitrogen-doped Porous Carbon from Urea via Magnesiothermic Reduction. *Carbon* **2018**, *130*, 41–47. [[CrossRef](#)]
5. Corsi, J.S.; Welborn, S.S.; Stach, E.A.; Detsi, E. Insights into the Degradation Mechanism of Nanoporous Alloy-Type Li-Ion Battery Anodes. *ACS Energy Lett.* **2021**, *6*, 1749–1756. [[CrossRef](#)]
6. He, J.; Wei, Y.Q.; Hu, L.T.; Li, H.Q.; Zhai, T.Y. Aqueous Binder Enhanced High-Performance GeP5 Anode for Lithium-Ion Batteries. *Front. Chem.* **2018**, *6*, 2121. [[CrossRef](#)]

7. Jiang, T.; Ma, S.Y.; Deng, J.B.; Yuan, T.; Lin, C.F.; Liu, M.L. Partially Reduced Titanium Niobium Oxide: A High-Performance Lithium-Storage Material in a Broad Temperature Range. *Adv. Sci.* **2021**, *9*, 2105119. [CrossRef]
8. Li, Q.; Li, H.S.; Xia, Q.T.; Hu, Z.Q.; Zhu, Y.; Yan, S.S.; Ge, C.; Zhang, Q.H.; Wang, X.X.; Shang, X.T.; et al. Extra Storage Capacity in Transition Metal Oxide Lithium-ion Batteries Revealed by in Situ Magnetometry. *Nat. Mater.* **2021**, *20*, 76–83. [CrossRef]
9. Chakraborty, G.; Park, I.H.; Medishetty, R.; Vittal, J.J. Two-Dimensional Metal-Organic Framework Materials: Synthesis, Structures, Properties and Applications. *Chem. Rev.* **2021**, *121*, 3751–3891. [CrossRef]
10. Yao, M.S.; Li, W.H.; Xu, G. Metal-organic Frameworks and Their Derivatives for Electrically-transduced Gas sensors. *Coord. Chem. Rev.* **2021**, *426*, 213479213479. [CrossRef]
11. Dybtsev, D.N.; Bryliakov, K.P. Asymmetric Catalysis Using Metal-organic Frameworks. *Coord. Chem. Rev.* **2021**, *437*, 213845213845. [CrossRef]
12. Cai, W.; Wang, J.Q.; Chu, C.C.; Chen, W.; Wu, C.S.; Liu, G. Metal Organic Framework-Based Stimuli-Responsive Systems for Drug Delivery. *Adv. Sci.* **2019**, *6*, 18015261801526. [CrossRef] [PubMed]
13. Wang, D.; Zhou, W.W.; Zhang, R.; Huang, X.X.; Zeng, J.J.; Mao, Y.F.; Ding, C.Y.; Zhang, J.; Liu, J.P.; Wen, G.W. MOF-derived Zn-Mn Mixed oxides@carbon Hollow Disks with Robust Hierarchical Structure for High-performance lithium-ion Batteries. *J. Mater. Chem. A* **2018**, *6*, 2974–2983. [CrossRef]
14. Zheng, M.B.; Tang, H.; Li, L.L.; Hu, Q.; Zhang, L.; Xue, H.G.; Pang, H. Hierarchically Nanostructured Transition Metal Oxides for Lithium-Ion Batteries. *Adv. Sci.* **2018**, *5*, 17005921700592. [CrossRef] [PubMed]
15. Wang, Y.Y.; Zhang, M.; Li, S.L.; Zhang, S.R.; Xie, W.; Qin, J.S.; Su, Z.M.; Lan, Y.Q. Diamondoid-structured Polymolybdate-based Metal-organic Frameworks as High-capacity Anodes for lithium-ion Batteries. *Chem. Commun.* **2017**, *53*, 5204–5207. [CrossRef]
16. Zhang, Y.; Niu, Y.B.; Liu, T.; Li, Y.T.; Wang, M.Q.; Hou, J.K.; Xu, M.W. A nickel-based Metal-organic Framework: A novel optimized Anode Material for Li-ion Batteries. *Mater. Lett.* **2015**, *161*, 712–715. [CrossRef]
17. Gong, T.; Lou, X.B.; Gao, E.Q.; Hu, B.W. Pillared-Layer Metal Organic Frameworks for Improved Lithium-Ion Storage Performance. *ACS Appl. Mater. Interfaces* **2017**, *9*, 21839–21847. [CrossRef]
18. Li, X.X.; Cheng, F.Y.; Zhang, S.N.; Chen, J. Shape-controlled Synthesis and lithium-storage Study of Metal-organic Frameworks $Zn_4O(1,3,5\text{-benzenetribenzoate})_2$. *J. Power Sources* **2006**, *160*, 542–547. [CrossRef]
19. Wang, P.; Lou, X.B.; Li, C.; Hu, X.S.; Yang, Q.; Hu, B.W. One-Pot Synthesis of Co-Based Coordination Polymer Nanowire for Li-Ion Batteries with Great Capacity and Stable Cycling Stability. *Nano-Micro Lett.* **2018**, *10*, 1919. [CrossRef]
20. Yang, J.; Zheng, C.; Xiong, P.X.; Li, Y.F.; Wei, M.D. Zn-doped Ni-MOF Material with a High Supercapacitive Performance. *J. Mater. Chem. A* **2014**, *2*, 19005–19010. [CrossRef]
21. Liu, H.; Cao, Q.; Fu, L.J.; Li, C.; Wu, Y.P.; Wu, H.Q. Doping effects of zinc on LiFePO₄ Cathode Material for lithium ion Batteries. *Electrochem. Commun.* **2006**, *8*, 1553–1557. [CrossRef]
22. Raju, K.; Venkataiah, G.; Yoon, D.H. Effect of Zn Substitution on the Structural and Magnetic Properties of Ni-Co ferrites. *Ceram. Int.* **2014**, *40*, 9337–9344. [CrossRef]
23. Han, X.Y.; Qing, G.Y.; Sun, J.T.; Sun, T.L. How Many Lithium Ions Can Be Inserted onto Fused C₆ Aromatic Ring Systems. *Angew. Chem.* **2011**, *124*, 5237–5241. [CrossRef]
24. Lee, G.; Varanasi, C.V.; Liu, J. Effects of Morphology and Chemical Doping on Electrochemical Properties of Metal Hydroxides in Pseudocapacitors. *Nanoscale* **2015**, *7*, 3181–3188. [CrossRef] [PubMed]
25. Niu, Y.B.; Xu, M.W.; Cheng, C.J.; Bao, S.J.; Hou, J.K.; Liu, S.G.; Yi, F.L.; He, H.; Li, C.M. Na_{3.12}Fe_{2.44}(P₂O₇)₂/multi-walled Carbon Nanotube Composite as a Cathode Material for Sodium-ion Batteries. *J. Mater. Chem. A* **2015**, *3*, 17224–17229. [CrossRef]
26. Rahdar, A.; Aliahmad, M.; Azizi, Y. NiO Nanoparticles: Synthesis and Characterization. *J. Nanostruct.* **2015**, *5*, 145–151. Available online: <https://www.sid.ir/en/journal/ViewPaper.aspx?id=490392> (accessed on 1 June 2015).
27. Xiong, G.; Pal, U.; Serrano, J.G.; Ucer, K.B.; Williams, R.T. Photoluminescence and FTIR study of ZnO Nanoparticles: The Impurity and Defect Perspective. *Phys. Status Solidi C* **2006**, *3*, 3577–3581. [CrossRef]
28. Chen, J.; Liu, R.; Gao, H.; Chen, L.; Ye, D. Amine-functionalized Metal-organic Frameworks for the Transesterification of Triglycerides. *J. Mater. Chem. A* **2014**, *2*, 7205–7213. [CrossRef]
29. Fomekong, R.L.; Tsobnang, P.K.; Magnin, D.; Hermans, S.; Delcorte, A.; Ngolui, J.L. Coprecipitation of Nickel zinc malonate: A facile and reproducible synthesis route for Ni_{1-x}Zn_xO nanoparticles and Ni_{1-x}Zn_xO/ZnO nanocomposites via pyrolysis. *J. Solid State Chem.* **2015**, *230*, 381–389. [CrossRef]
30. Yan, Y.; Lin, J.; Cao, J.; Guo, S.; Zheng, X.; Feng, J.; Qi, J. Activating and Optimizing the Activity of NiCoP Nanosheets for Electrocatalytic Alkaline Water Splitting Through the V doping Effect Enhanced by P vacancies. *J. Mater. Chem. A* **2019**, *7*, 24486–24492. [CrossRef]
31. Zhang, J.H.; Cai, G.F.; Zhou, D.; Tang, H.; Wang, X.L.; Gu, C.D.; Tu, J.P. Co-doped NiO nanoflake Array Films with Enhanced Electrochromic Properties. *J. Mater. Chem. C* **2014**, *2*, 7013–7021. [CrossRef]
32. Zhao, L.L.; Su, G.; Liu, W.; Cao, L.X.; Wang, J.; Dong, Z.; Song, M.Q. Optical and Electrochemical Properties of Cu-doped NiO Films Prepared by Electrochemical Deposition. *Appl. Surf. Sci.* **2011**, *257*, 3974–3979. [CrossRef]
33. Armand, M.; Grugeon, S.; Vezin, H.; Laruelle, S.; Ribiere, P.; Poizot, P.; Tarascon, J.M. Conjugated Dicarboxylate anodes for Li-ion Batteries. *Nat. Mater.* **2009**, *8*, 120–125. [CrossRef] [PubMed]

34. Li, C.; Hu, X.; Lou, X.; Zhang, L.; Wang, Y.; Amoureux, J.-P.; Shen, M.; Chen, Q.; Hu, B. The Organic-moiety-dominated Li⁺ InterCalation/deintercalation Mechanism of a Cobalt-based Metal-organic Framework. *J. Mater. Chem. A* **2016**, *4*, 16245–16251. [[CrossRef](#)]
35. Wang, L.; Yu, Y.; Chen, P.C.; Zhang, D.W.; Chen, C.H. Electrospinning Synthesis of C/Fe₃O₄ Composite Nanofibers and their Application for High Performance lithium-ion batteries. *J. Power Sources* **2008**, *183*, 717–723. [[CrossRef](#)]
36. Chen, P.; Wu, Z.; Guo, T.; Zhou, Y.; Liu, M.; Xia, X.; Sun, J.; Lu, L.; Ouyang, X.; Wang, X.; et al. Strong Chemical Interaction between Lithium Polysulfides and Flame-Retardant Polyphosphazene for Lithium-Sulfur Batteries with Enhanced Safety and Electrochemical Performance. *Adv. Mater.* **2021**, *33*, e2007549. [[CrossRef](#)] [[PubMed](#)]
37. Qin, B.; Cai, Y.; Si, X.; Li, C.; Cao, J.; Fei, W.; Qi, J. Ultra-lightweight ion-sieving Membranes for High-rate lithium Sulfur Batteries. *Chem. Eng. J.* **2022**, *430*, 132698. [[CrossRef](#)]
38. Zhou, G.; Tian, H.; Jin, Y.; Tao, X.; Liu, B.; Zhang, R.; Seh, Z.W.; Zhuo, D.; Liu, Y.; Sun, J.; et al. Catalytic Oxidation of Li₂S on the Surface of Metal Sulfides for Li-S Batteries. *Proc. Natl. Acad. Sci. USA* **2017**, *114*, 840–845. [[CrossRef](#)]
39. Qi, J.; Yan, Y.; Cai, Y.; Cao, J.; Feng, J. Nanoarchitected Design of Vertical-Standing Arrays for Supercapacitors: Progress, Challenges, and Perspectives. *Adv. Funct. Mater.* **2020**, *31*, 2006030. [[CrossRef](#)]
40. Rui, Z.; Jie, L.; Gu, J. The Effects of Electrode Thickness on the Electrochemical and Thermal Characteristics of Lithium-ion Battery. *Appl. Energy* **2015**, *139*, 220–229. [[CrossRef](#)]
41. Senthil Kumar, R.; Nithya, C.; Gopukumar, S.; Anbu Kulandainathan, M. Diamondoid-Structured Cu-Dicarboxylate-based Metal-Organic Frameworks as High-Capacity Anodes for Lithium-Ion Storage. *Energy Technol.* **2014**, *2*, 921–927. [[CrossRef](#)]
42. Tang, B.; Huang, S.; Fang, Y.; Hu, J.; Malonzo, C.; Truhlar, D.G.; Stein, A. Mechanism of electrochemical lithiation of a metal-organic framework without redox-active nodes. *J. Chem. Phys.* **2016**, *144*, 194702. [[CrossRef](#)]
43. Han, X.; Yi, F.; Sun, T.; Sun, J. Synthesis and electrochemical performance of Li and Ni 1,4,5,8-naphthalenetetracarboxylates as anodes for Li-ion batteries. *Electrochem. Commun.* **2012**, *25*, 136–139. [[CrossRef](#)]
44. Lin, Y.; Zhang, Q.; Zhao, C.; Li, H.; Kong, C.; Shen, C.; Chen, L. An exceptionally stable functionalized metal-organic framework for lithium storage. *Chem. Commun.* **2015**, *51*, 697–699. [[CrossRef](#)] [[PubMed](#)]
45. Li, G.; Li, F.; Yang, H.; Cheng, F.; Xu, N.; Shi, W.; Cheng, P. Graphene oxides doped MIL-101(Cr) as anode materials for enhanced electrochemistry performance of lithium ion battery. *Inorg. Chem. Commun.* **2016**, *64*, 63–66. [[CrossRef](#)]
46. Hu, L.; Lin, X.M.; Mo, J.T.; Lin, J.; Gan, H.L.; Yang, X.L.; Cai, Y.P. Lead-Based Metal-Organic Framework with Stable Lithium Anodic Performance. *Inorg. Chem.* **2017**, *56*, 4289–4295. [[CrossRef](#)]
47. Saravanan, K.; Nagarathinam, M.; Balaya, P.; Vittal, J.J. Lithium storage in a metal organic framework with diamondoid topology—A case study on metal formates. *J. Mater. Chem.* **2010**, *20*, 8329–8335. [[CrossRef](#)]
48. Liu, Q.; Yu, L.; Wang, Y.; Ji, Y.; Horvat, J.; Cheng, M.L.; Jia, X.; Wang, G. Manganese-based layered coordination polymer: Synthesis, structural characterization, magnetic property, and electrochemical performance in lithium-ion batteries. *Inorg. Chem.* **2013**, *52*, 2817–2822. [[CrossRef](#)]
49. Li, H.; Su, Y.; Sun, W.; Wang, Y. Carbon Nanotubes Rooted in Porous Ternary Metal Sulfide@N/S-Doped Carbon Dodecahedron: Bimetal-Organic-Frameworks Derivation and Electrochemical Application for High-Capacity and Long-Life Lithium-Ion Batteries. *Adv. Funct. Mater.* **2016**, *26*, 8345–8353. [[CrossRef](#)]
50. Zhou, D.; Ni, J.; Li, L. Self-supported multicomponent CPO-27 MOF nanoarrays as high-performance anode for lithium storage. *Nano Energy* **2019**, *57*, 711–717. [[CrossRef](#)]
51. Xia, S.-B.; Yu, S.-W.; Yao, L.-F.; Li, F.-S.; Li, X.; Cheng, F.-X.; Shen, X.; Sun, C.-K.; Guo, H.; Liu, J.-J. Robust hexagonal nut-shaped titanium(IV) MOF with porous structure for ultra-high performance lithium storage. *Electrochim. Acta* **2019**, *296*, 746–754. [[CrossRef](#)]